Collin J. C. Epstein[1]
Sandia National Laboratories,
Albuquerque, NM 87123
e-mail: cepstei@sandia.gov

Ryan N. Goodner
Sandia National Laboratories,
Albuquerque, NM 87123
e-mail: rngoodn@sandia.gov

R. Derek West
Sandia National Laboratories,
Albuquerque, NM 87123
e-mail: rdwest@sandia.gov

Kyle R. Thompson
Sandia National Laboratories,
Albuquerque, NM 87123
e-mail: krthomp@sandia.gov

Amber L. Dagel
Sandia National Laboratories,
Albuquerque, NM 87123
e-mail: aldagel@sandia.gov

Influence of Data Acquisition Algorithms on X-Ray Phase Contrast Imaging Computed Tomography

X-ray phase contrast imaging (XPCI) is a nondestructive evaluation technique that enables high-contrast detection of low-attenuation materials that are largely transparent in traditional radiography. Extending a grating-based Talbot-Lau XPCI system to three-dimensional imaging with computed tomography (CT) imposes two motion requirements: the analyzer grating must translate transverse to the optical axis to capture image sets for XPCI reconstruction, and the sample must rotate to capture angular data for CT reconstruction. The acquisition algorithm choice determines the order of movement and positioning of the two stages. The choice of the image acquisition algorithm for XPCI CT is instrumental to collecting high fidelity data for reconstruction. We investigate how data acquisition influences XPCI CT by comparing two simple data acquisition algorithms and determine that capturing a full phase-stepping image set for a CT projection before rotating the sample results in higher quality data. [DOI: 10.1115/1.4048517]

Keywords: imaging, radiography, testing methodologies, X-ray, computed tomography, X-ray phase contrast imaging, Talbot-Lau interferometer

1 Introduction

X-ray phase contrast imaging (XPCI) is a radiography technique that leverages the wave properties of X-rays to obtain phase contrast data in addition to traditional absorption contrast data. In the hard X-ray regime, the phase cross section can exceed the attenuation cross section by up to three orders of magnitude for elements with low atomic numbers [1,2]. Volumetric reconstructions of XPCI data can be reconstructed using computed tomography (CT) techniques [3,4], which include capturing numerous angular samples of a rotating object.

We implement a table-top grating-based XPCI system with a laboratory tube source using a Talbot-Lau interferometer [5] (Fig. 1). XPCI reconstruction results in three image products: tau, dark field, and differential phase (Fig. 2). The tau image is equivalent to traditional attenuation-contrast radiography, the dark field image is due to small-angle scatter, and the differential phase image reveals material interfaces. The differential phase image may be integrated to yield an absolute phase image.

The combination of interferometer motion required for grating-based XPCI and sample rotation mandated by CT dictates at least two distinct image acquisition techniques: capture an entire phase image set before rotating the object to a new angle and capture a full rotational projection set before phase-stepping the analyzer grating. We compare two simple data acquisition techniques and their influence on resulting XPCI CT reconstructions.

The sample object is a paper cup containing numerous 1/2 in. (12.7 mm) diameter plastic spheres (Fig. 2). The spheres are composed of six different materials: nylon, clear acrylic, polyamide-imide Torlon, Delrin acetyl resin, and polypropylene.

2 Background

2.1 X-Ray Phase Contrast Imaging. Current X-ray detector technology cannot directly measure phase. The Talbot-Lau interferometer instead transforms phase information into a periodic intensity fringe pattern that the detector can measure, which enables phase reconstruction.

The source grating G0 divides a finite incoherent X-ray source into a set of smaller individually coherent (yet mutually incoherent) sources. The phase grating G1 imposes a periodic phase shift of magnitude π on the wavefront, creating an interference pattern across the detector. The analyzer grating G2 samples the interference pattern and produces an observable moiré fringe pattern on the detector [6,7].

Phase reconstruction with this apparatus requires the acquisition of a sequence of images captured as the analyzer grating G2 is stepped transverse to the optical axis. The movement of G2 causes lateral movement of the fringe pattern. We capture the

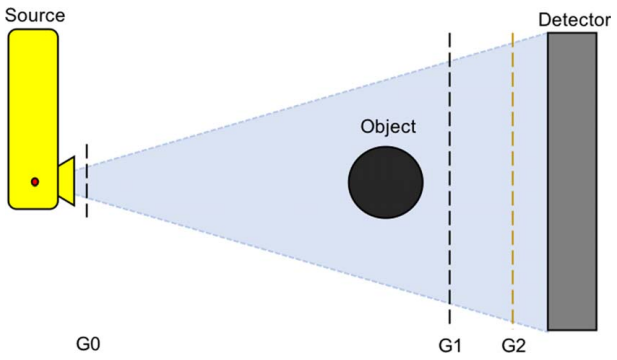

Fig. 1 Grating-based XPCI CT apparatus diagram (top view). Analyzer grating G2 steps transversely to the beam to capture phase data. Object rotates to capture angular samples for volume data.

[1]Corresponding author.

Manuscript received October 31, 2019; final manuscript received September 14, 2020; published online October 15, 2020. Assoc. Editor: Xiuming Wang.

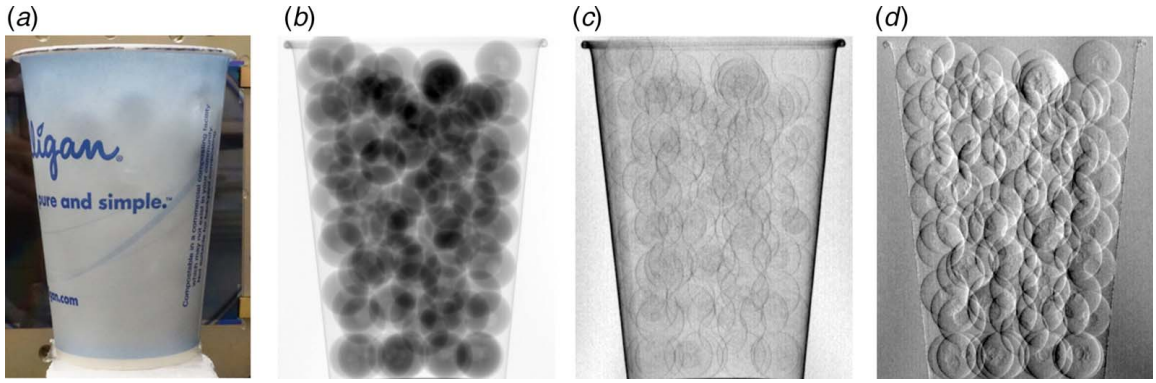

Fig. 2 Sample: small plastic spheres in paper cup. A single XPCI dataset yields three distinct reconstructed images. (*a*) Photograph, (*b*) tau, (*c*) dark field, and (*d*) differential phase.

requisite images for XPCI reconstruction by translating the grating over a full grating period at regular intervals and capturing a radiograph at each grating position. This process, known as phase stepping [8], samples the fringe pattern and must be completed for both reference and sample image sets. The number of phase steps is dictated by the Shannon–Nyquist Theorem [9].

The simplest method of reconstructing XPCI image products from phase-stepped data employs a fast Fourier transform (FFT). The grayscale value of each pixel in the radiograph changes with the translation of G2. We assume a sinusoidal signal model for the pixel modulation:

$$f = A\,\sin(\omega x + \phi) + b \tag{1}$$

and estimate the sinusoid parameters at each pixel location with an FFT.

The XPCI image products are created by measuring how the sinusoid fitted to each pixel changes between the sample and reference signals. Absorption images (τ) are computed from the DC offsets. Dark field (DF) images illustrate visibility modulation and are computed from the sinusoid amplitude, normalized by the computed absorption. For horizontally stepped G2 gratings, the differential phase images (dP) illustrate the horizontally induced refraction and is computed as the difference of phase terms.

$$\tau = \frac{b_S}{b_R} \tag{2}$$

$$DF = \frac{A_S}{A_R} \times \frac{b_R}{b_S} \tag{3}$$

$$dP = \phi_S - \phi_R \tag{4}$$

In these equations, the subscript indicates whether the sinusoid parameter value is derived from the sample (S) or reference (R) image. With the FFT method, XPCI reconstruction quality heavily depends on the fidelity of the sinusoidal fit, which in turn depends on the data sampling period and uniformity.

2.2 Computed Tomography. CT refers to the reconstruction of a set of two-dimensional radiographs captured at multiple angular rotations, or projections, into a set of images depicting planar views within the volume of interest. These images are known as slices. A set of parallel slices at different heights provides a volumetric representation of the scanned object. The inputs to the CT reconstruction algorithm are the system geometry parameters and the corresponding set of rotational projections captured over (ideally) 360 deg of rotation. The number of projections P required to resolve the highest frequency features in a volume with maximum width D pixels on a detector is calculated by applying the Shannon–Nyquist Theorem to image data:

$$P \geq D \times \frac{\pi}{2} \tag{5}$$

We employ the traditional Feldkamp–Davis–Kress analytic algorithm [10] to reconstruct the CT data.

3 Apparatus

All gratings used in the Sandia National Laboratories (SNL) laboratory grating-based three-dimensional X-ray phase contrast imaging system were fabricated at the Microsystems Engineering, Science and Applications (MESA) facility at SNL [11]. The grating features are summarized in Table 1.

The X-ray source is a Philips MG 225 kV laboratory bench-top mini-focus tube source operated at tube potential $V = 41\ kV_p$ and current $I = 15$ mA. The detector is a PaxScan® 1313DX digital image receptor from Varex Imaging Corporation with 1024×1024 pixels and pixel pitch $p = 127\ \mu$m operated in 2×2 binning mode. The entire system is mounted on a floating optical table to minimize vibrations. A detailed description of the grating-based XPCI CT system used in this investigation is available in the study by Thompson et al. [12].

4 Data Acquisition Algorithms

X-ray phase contrast imaging CT requires the acquisition of radiographs that satisfy both XPCI and CT reconstruction requirements. The image data set must include sufficient projection image sets for CT reconstruction, and each projection set must contain radiographs adequate for XPCI reconstruction of that projection. Therefore, data acquisition algorithms must coordinate two mechanical stages: the analyzer grating G2 horizontal translation stage and the sample rotational mount.

The motion requirements for XPCI CT indicate that each stage may be considered as a motion loop, a set of movements that could occur repeatedly. The organization of potential data acquisition algorithms then follow a nested loop form in which one motion

Table 1 Summary of grating dimensions

Grating	Area (mm^2)	Period (μm)	Material
G0	10×10	88	Au
G1	100×100	3.8735	Si
G2	100×100	1.981	Au

loop executes within the other. Two acquisition algorithms are then readily apparent: in one, sample rotation is the outer loop and grating translation is the inner loop, and vice versa in the other. Other data acquisition algorithms for XPCI CT have been explored, including interlaced grating translation [13,14], helical XPCI CT [15], and no grating movement at all [16]. We consider the two simple nested loop algorithms, which we call *Step First* and *Rotate First*. In our implementation, the angular positions of the sample stage and the phase step positions of the analyzer grating G2 for both motion loops are calculated with an arithmetic progression rather than relative to the previous position to prevent accumulation of position errors.

Theoretically, the two data acquisition techniques capture the same images but in a different order. Nevertheless, there are distinct advantages and disadvantages to each algorithm. If a *Step First* scan fails and does not capture a complete XPCI CT image set, the incomplete data include a subset of projections with complete data for XPCI reconstruction. In the event that a sufficient number of complete projections were captured, a limited-angle CT scan of that data set can be reconstructed. Conversely, a failed *Rotate First* scan results in an incomplete data set that cannot be reconstructed into XPCI image products since no individual projection contains a complete fringe profile for XPCI reconstruction. A traditional absorption CT scan may be reconstructed from a single sample rotation. Only the absorption image is available, and the visible fringes introduce significant reconstruction artifacts. However, *Rotate First* offers the potential for shorter scan times compared to *Step First*. If the scan runs at a high frame rate, *Rotate First* may rotate the sample continuously, with G2 translating to the next position at the conclusion of each sample revolution.

In practice, the data captured by the two acquisition algorithms differ slightly due to the system error. Numerous potential hardware challenges that introduce acquisition error exist in a laboratory grating-based XPCI system, such as X-ray source fluctuation, detector electronic noise, system thermal drift, mechanical and acoustic disturbances, and phase stepping errors [17]. Acquisition algorithm choice may exacerbate or mitigate certain error sources.

4.1 Step First: Outer Rotation, Inner Translation. We refer to the acquisition algorithm that rotates the sample in the outer loop and translates G2 in the inner loop as *Step First*. In *Step First*, a complete image set required for XPCI reconstruction for a given projection is acquired before rotating to the next projection. When the object is rotated, G2 is reset to its initial position. The process repeats for all projections required for CT reconstruction (Fig. 3(*a*)). Pseudocode describing the *Step First* algorithm is presented in Algorithm 1.

Algorithm 1 *Step First* acquisition algorithm

Input: User-defined acquisition parameters
Output: XPCI CT image set
1: **for** $i := 0$ to *projections* **do**
2: move rotary stage to *i*th projection angle
3: **for** $j := 0$ to *phase-steps* **do**
4: move analyzer grating stage to *j*th phase step position
5: acquire radiograph
6: **end for**
7: **end for**

4.2 Rotate First: Outer Translation, Inner Rotation. The algorithm that translates G2 in the outer loop and rotates the sample in the inner loop is named *Rotate First*. All the projections required for a CT scan are acquired for a given grating position. G2 then translates to the next position, repeating until the entire image set is captured (Fig. 3(*b*)). Algorithm 2 outlines *Rotate First* in pseudocode.

Algorithm 2 *Rotate First* acquisition algorithm

Input: User-defined acquisition parameters
Output: XPCI CT image set
1: **for** $i := 0$ to *phase-steps* **do**
2: move analyzer grating stage to *i*th phase step position
3: **for** $j := 0$ to *projections* **do**
4: move rotary stage to *j*th projection angle
5: acquire radiograph
6: **end for**
7: **end for**

5 Results

5.1 Fringe Signal Fidelity. As described in Sec. 2.1, XPCI reconstruction with the FFT method depends heavily on the fidelity of the underlying signal. If the signal is sinusoidal, the phase steps are evenly spaced and the steps occur over exactly one G2 grating period, then the FFT method is reasonably accurate. Figure 4 displays the sampled fringe data for a reference XPCI

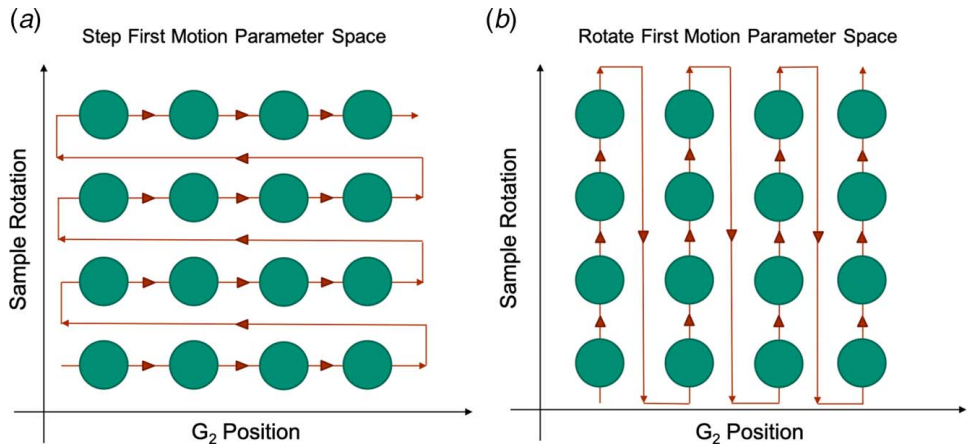

Fig. 3 Graphical representations of the traversal of parameter space during an XPCI CT scan: (*a*) visualization of *Step First* algorithm progression and (*b*) visualization of *Rotate First* algorithm progression

image set, a set acquired during a *Step First* scan and a set acquired during a *Rotate First* scan. The sampled pixel is located away from the sample toward the edge of the field of view for direct comparison between reference and sample sinusoids. Therefore, in the absence of system errors, all three fringe profiles should look similar and have roughly the same amplitude, phase, and offset. The fringe profile from the *Rotate First* scan is noticeably degraded compared to the reference and *Step First* profiles. Both fringe profiles also exhibit the significant phase shift relative to the reference signal. The degradation and the aberrant phase shift are likely due to a combination of the hardware errors articulated previously.

Degraded fringe profiles result in reconstruction errors in the resulting XPCI images. The errors are compounded when the images are used for CT reconstruction.

The fringe degradation effect is more pronounced for longer scans. Potential causes include mechanical and/or thermal drift, imprecise, unrepeatable G2 stage motion and flat-field calibrations expiring toward the end of a long scan.

We assess the quality of grating-based XPCI data by calculating the sinusoidal purity. As described in Sec. 2.1, the fringe profile is modeled as a pure sinusoid with a single frequency. In practice, other frequencies deform the signal. The sinusoidal purity is the proportion of the waveform that is due to the dominant frequency. Therefore, the metric measures how much the zero-mean fringe profile is degraded compared to the theoretically ideal signal and is calculated pixel by pixel. For a given pixel fringe profile x, we calculate an FFT, denoted as $\hat{f}(x)$. The purity is then calculated as follows:

$$P(x) = \frac{|c_1(x)|}{\sum_{i=1}^{n} |c_i(x)|} \tag{6}$$

where $c_i(x)$ is the ith complex coefficient of $\hat{f}(x)$ and n is the number of positive-valued terms in $\hat{f}(x)$. The DC offset value $c_0(x)$ is omitted since the offset is unrelated to the frequency composition of the signal (and is in fact 0 for zero-mean sinusoidal signals). Values of $P(x) \to 1$ indicate a pure sinusoid and values of $P(x) \to 0$ indicate severe signal degradation.

Sinusoidal purity is simple to calculate during reconstruction because the FFT reconstruction calculates and subsequently discards the higher-order coefficients. High purity indicates low error in G2 position and translation during data acquisition.

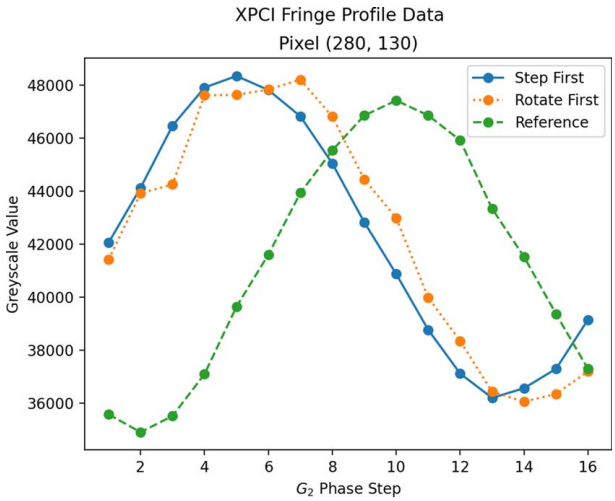

Fig. 4 Comparison of example profiles from pixel (280, 130) (image field of view 380 × 380), projection 225/451. A theoretically ideal fringe profile is a pure sinusoid. The clear degradation of the signal in the *Rotate First* scan indicates low-quality XPCI data and likely reconstruction errors.

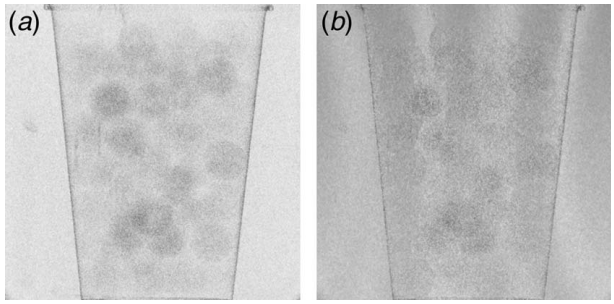

Fig. 5 Sinusoidal purity images calculated for projection 225/451: (*a*) *Step First* and (*b*) *Rotate First*. *Rotate First* image is noticeably darker, indicating lower purity. *Rotate First* image also exhibits residual fringes in the background that are absent in the *Step First* image.

Resampling the raw data may improve signal purity by correcting for phase-stepping errors [18].

Figure 5 shows the example of sinusoidal purity images calculated for example slices of data acquired with the *Step First* and *Rotate First* algorithms. The value $P(x) = 1$ is coded white, so brighter pixels indicate higher purity data. The *Step First* image is noticeably brighter than the *Rotate First* image, with a mean Purity of $\bar{P}_{step} = 0.8167$ compared to $\bar{P}_{rotate} = 0.6969$. A lower purity value and dimmer image indicate that the *Rotate First* algorithm captures lower quality XPCI data. The *Rotate First* image also contains a residual background fringe pattern, an indication of misalignment with the reference image set. Misalignment is likely due to the accumulation of phase-stepping errors over the protracted period of time required to acquire a full phase projection set.

The *Step First* algorithm consistently yields higher sinusoidal purity values than the *Rotate First* algorithm. We examined the purity images reconstructed from 4 XPCI CT scans (2 *Step First*, 2 *Rotate First*) acquired of the same plastic spheres sample, with the same acquisition parameters. We acquired 451 angular projects with 16 phase steps per projection for each scan. The reconstructed field of view is 380 × 380 pixels. The pixels from the images acquired with the *Step First* have a mean purity of $\mu_S = 0.8144$ with a standard deviation of $\sigma_S = 0.0676$. The *Rotate First* scans result in a mean pixel purity of $\mu_R = 0.6986$ with a standard deviation of $\sigma_R = 0.0687$. Thus, *Step First* reliably captures higher quality grating-based XPCI data in aggregate.

5.2 Sinogram Intensity Variation. The influence of acquisition algorithm on reconstructed data is most apparent in the

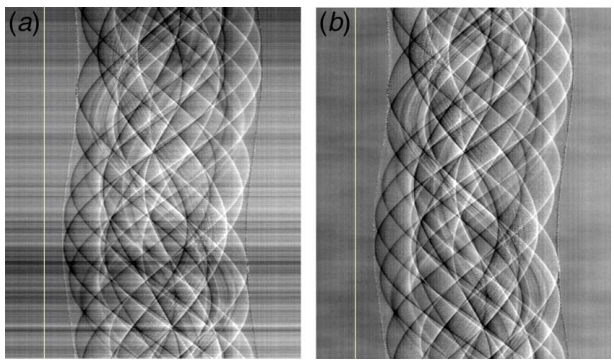

Fig. 6 Differential phase CT signograms, slice 185/451: (*a*) *Step First* and (*b*) *Rotate First*. The sinogram for *Step First* data noticeably varies in intensity. Vertical line indicates profile location plotted in Fig. 7 (column 50/380).

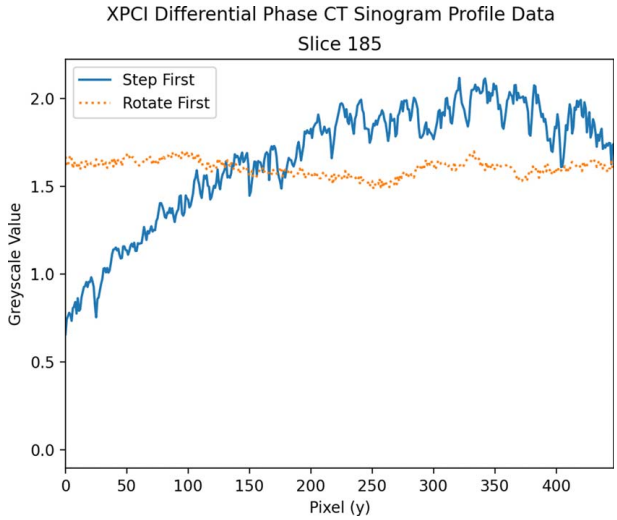

Fig. 7 Differential phase sinogram profiles of background phase regions as indicated in Fig. 6 (slice 185/451, column 50/380). *Step First* exhibits large phase variability compared to *Rotate First*.

differential phase modality. Differential phase images reconstructed from the data acquired with *Step First* vary in intensity over the course of the scan, while the images reconstructed from corresponding *Rotate First* data have relatively constant intensity. The intensity variation effect is most easily observed by examining the sinograms of the respective differential phase data sets (Fig. 6). A profile plot reveals a net background shift of about $\pi/2$ over the course of the *Step First* scan, compared to almost no phase shift during the *Rotate First* scan (Fig. 7). Recall that the differential phase value is due to the phase difference between reference and sample fringe profiles (e.g., see Fig. 4).

Projection intensity variability is a common problem in traditional CT. Fluctuations in the output of the X-ray source during a CT scan can cause projections to differ in brightness. We observe a similar phenomenon in *Step First* data, but not *Rotate First* data. While individual projections may have a more regular phase profile using *Step First*, the shift in the background phase between projections may be substantial. During a *Rotate First* scan, phase-stepping images in each fringe profile are acquired over the duration of the scan. The temporal spread effectively averages background phase, resulting in a more stable value across projections.

Existing CT reconstruction algorithms normalize projections to account for source intensity fluctuations. When applied to the differential phase data, the traditional normalization produces reconstructions that appear correct. However, the cause of apparent intensity variation in differential phase images is actually background phase shift, not X-ray beam intensity. The mechanism causing the error is located in G2 translation repeatability rather than X-ray source instability. Therefore, the traditional projection normalization used in CT reconstruction may be inappropriate for correcting differential phase data because it targets a different physical phenomenon. Further investigation is required to determine whether the background phase shift between projections is best addressed through hardware improvements or software postprocessing techniques.

6 Conclusion

X-ray phase contrast imaging CT using a grating-based Talbot-Lau interferometer system requires multiple moving stages to acquire the requisite data for successful reconstruction. Coordination of those stages demands deliberate attention to the design of data acquisition algorithms and their effects on the captured data.

While the choice of whether to place grating translation or sample rotation in the inner or outer acquisition loops primarily determines the order in which scan images are captured, it also influences the XPCI CT reconstruction. The *Step First* algorithm acquires higher fidelity fringe profiles as evidenced by the consistently higher purity of *Step First* data. However, the *Step First* technique is more vulnerable to background phase shifts than the *Rotate First* algorithm.

Step First results in XPCI CT data sets that can be salvaged if a scan fails and delivers superior sinusoidal profiles and resulting XPCI reconstructions. We therefore prefer *Step First* when pursuing high-quality volume data.

An investigation of the causes of fringe profile degradation may help mitigate observed artifacts. Potential system error sources include G2 phase-stepping error, system thermal drift, and vibration sensitivity. Fringe profile degradation may also be addressed with postprocessing techniques such as phase-stepping position resampling and background phase shift normalization or minimization.

Acknowledgment

This article describes objective technical results and analysis. Any subjective views or opinions that might be expressed do not necessarily represent the views of the U.S. Department of Energy or the United States Government.

This work was supported by the Laboratory Directed Research and Development program at Sandia National Laboratories. Sandia National Laboratories is a multimission laboratory managed and operated by National Technology & Engineering Solutions of Sandia, LLC, a wholly owned subsidiary of Honeywell International Inc., for the U.S. Department of Energy's National Nuclear Security Administration under contract DE-NA0003525. SAND2020-8573 J.

Conflict of Interest

There are no conflicts of interest.

References

[1] Momose, A., 2005, "Recent Advances in X-Ray Phase Imaging," Jpn. J. Appl. Phys., **44**(9A), pp. 6355–6367.
[2] Endrizzi, M., 2018, "X-Ray Phase-Contrast Imaging," Nucl. Instrum. Methods Phys. Res. Sect. A: Acceler., Spectrom., Detectors Assoc. Equip., **878**, pp. 88–98.
[3] Pfeiffer, F., Bunk, O., Kottler, C., and David, C., 2007, "Tomographic Reconstruction of Three-Dimensional Objects From Hard X-Ray Differential Phase Contrast Projection Images," Nucl. Instrum. Methods Phys. Res. Sect. A: Acceler., Spectrom., Detectors Assoc. Equip., **580**(2), pp. 925–928.
[4] Pfeiffer, F., Kottler, C., Bunk, O., and David, C., 2007, "Hard X-Ray Phase Tomography With Low-Brilliance Sources," Phys. Rev. Lett., **98**(10), p. 108105.
[5] Pfeiffer, F., Weitkamp, T., Bunk, O., and David, C., 2006, "Phase Retrieval and Differential Phase-Contrast Imaging With Low-Brilliance X-Ray Sources," Nat. Phys., **2**(4), p. 258.
[6] Pfeiffer, F., Bech, M., Bunk, O., Kraft, P., Eikenberry, E. F., Brönnimann, C., Grünzweig, C., and David, C., 2008, "Hard-X-Ray Dark-Field Imaging Using a Grating Interferometer," Nat. Mater., **7**(2), pp. 134–137.
[7] Pfeiffer, F., Bech, M., Bunk, O., Donath, T., Henrich, B., Kraft, P., and David, C., 2009, "X-Ray Dark-Field and Phase-Contrast Imaging Using a Grating Interferometer," J. Appl. Phys., **105**(10), pp. 1–4.
[8] Weitkamp, T., Diaz, A., David, C., Pfeiffer, F., Stampanoni, M., Cloetens, P., and Ziegler, E., 2005, "X-Ray Phase Imaging With a Grating Interferometer," Opt. Exp., **13**(16), pp. 6296–6304.
[9] Shannon, C. E., 1949, "Communication in the Presence of Noise," Proc. IRE, **37**(1), pp. 10–21.
[10] Feldkamp, L. A., Davis, L. C., and Kress, J. W., 1984, "Practical Cone-Beam Algorithm," Josa a, **1**(6), pp. 612–619.
[11] Finnegan, P. S., Hollowell, A. E., Arrington, C. L., and Dagel, A. L., 2019, "High Aspect Ratio Anisotropic Silicon Etching for X-Ray Phase Contrast Imaging Grating Fabrication," Mater. Sci. Semicond. Process., **92**, pp. 80–85.
[12] Thompson, K. R., Dagel, A., Goodner, R. N., and Epstein, C., 2019, "Progress on Building a Laboratory Based X-Ray Phase Contrast Imaging Computed Tomography System," AIP Conference Proceedings, Vermont, July 15–19, Vol. 2102, AIP Publishing LLC, p. 030001.
[13] Zanette, I., Bech, M., Pfeiffer, F., and Weitkamp, T., 2011, "Interlaced Phase Stepping in Phase-Contrast X-Ray Tomography," Appl. Phys. Lett., **98**(9), pp. 2009–2012.

[14] Zanette, I., Bech, M., Rack, A., Le Duc, G., Tafforeau, P., David, C., Mohr, J., Pfeiffer, F., and Weitkamp, T., 2012, "Trimodal Low-Dose X-Ray Tomography," Proc. Natl. Acad. Sci. USA, **109**(26), pp. 10199–10204.
[15] Fu, J., Willner, M., Chen, L., Tan, R., Achterhold, K., Bech, M., Herzen, J., Kunka, D., Mohr, J., and Pfeiffer, F., 2014, "Helical Differential X-Ray Phase-Contrast Computed Tomography," Phys. Medica, **30**(3), pp. 374–379.
[16] Bevins, N., Zambelli, J., Li, K., Qi, Z., and Chen, G. H., 2012, "Multicontrast X-Ray Computed Tomography Imaging Using Talbot-Lau Interferometry Without Phase Stepping," Medical Physics, **39**(1), pp. 424–428.
[17] Dagel, A. L., West, R. D., Goodner, R. N., Grover, S., Epstein, C., and Thompson, K., 2019, "Optimization of Hardware and Image Processing for Improved Image Quality in X-Ray Phase Contrast Imaging," SPIE Defense + Commercial Sensing, Baltimore, MD, Apr. 14–18, p. 109990S.
[18] Marco, F. D., Marschner, M., Birnbacher, L., Noël, P., Herzen, J., and Pfeiffer, F., 2018, "Analysis and Correction of Bias Induced by Phase Stepping Jitter in Grating-Based X-Ray Phase-Contrast Imaging," Opt. Express, **26**(10), pp. 12707–12722.